Rupture Directivity Effects of Large Seismic Sources, Case of February 6th 2023 Catastrophic Earthquakes in Turkey

O. V. Pavlenko[a], * and V. A. Pavlenko[a], *
[a] Schmidt Institute of Physics of the Earth, Moscow, 123995 Russia
**e-mail: olga@ifz.ru*
***e-mail: pavlenko.vasily@gmail.com*

Abstract—An overview of the results obtained by foreign seismologists based on the records of Turkish seismic networks AFAD (State Agency for Disaster Management under the Ministry of Internal Affairs) is presented. The sequence of earthquakes began with the $M7.8$ main shock and includes thousands of aftershocks. The strongest events occurred in the first twelve hours, with the sources of two $M7.0+$ events located 100 km apart. Earthquakes have caused ground motions that are destructive to structures, the so-called "pulse-like waveforms," and epicentral distances, as was previously noted, are not a good indicator of attenuation of waves from earthquakes with extended ruptures. The records of stations in the near-fault zones clearly revealed the directivity effects of seismic radiation. The $M7.8$ earthquake (main shock) was larger than expected in the current tectonic setting. The near-field records traced an early transition to the super-shear ($\sim 1.55 V_s$) rupture propagation on the Narli lateral fault, where the rupture originated and then passed into the East Anatolian fault. The early transition to the super-shear stage obviously contributed to the further propagation of the rupture and the initiation of slips on the East Anatolian fault. A dynamic fracture model has been constructed that matches the various results of inversions obtained by different authors and reveals spatially inhomogeneous rupture propagation velocities. Super-shear velocities exceeding the shear wave velocity V_s are observed along the Narli lateral fault and at the southwestern end of the East Anatolian fault. Since the late 1990s, seismologists have been working on incorporating the rupture directivity effects of extended sources into the probabilistic seismic hazard analysis procedures, but no consensus has been reached so far, and progress in this area can only be expected with the accumulation of a sufficient amount of observational data.

Keywords: earthquakes in Turkey of 2023, directivity effects of seismic radiation, pulse-like waveforms, ground motions prediction equations

DOI: 10.1134/S1069351323060149

INTRODUCTION

On February 6, 2023, at 4:17 local time (UTC+3), an earthquake of moment magnitude 7.8 occurred in Turkey's Gaziantep Province. The earthquake triggered a seismic sequence of hundreds of earthquakes of magnitudes above three, among which there were $M_w = 7.6$ and $M_w = 6.7$ events. The epicenter areas of the earthquakes extend for several hundred kilometres in the east of Turkey, towards the border with Syria; together with the North Anatolian Fault system and the western part of Turkey, these are the highest seismic hazard zones according to PSHA.

Figure 1 shows the Turkey seismic hazard map in terms of peak ground accelerations (PGA) on rock with a return period of ~475 years.

Baltzopoulos et al. (2023) have studied the Turkey seismic sequence. Table 1 from (Baltzopoulos et al., 2023) reports the coordinates of the epicenters of the three main events of the sequence, the hypocenter depth, and the fault mechanisms.

The main shock was followed by aftershocks; in the first twenty-four hours, there were, on average, about fifteen events an hour; their epicenters are shown in Fig. 2. No foreshocks were recorded.

Approximately ten minutes after the main shock and less than 25 km from its epicenter, a $M6.7$ event occurred. During the first hour, nine earthquakes of magnitude above five were recorded; for comparison, as many $M5.0+$ events were recorded during the long-lasting seismic sequence in Central Italy in 2016−2017 (Iervolino et al., 2021) but over five months.

The second largest $M7.5$ event of the series occurred approximately 100 km north of the main shock that was followed by five $M5.0+$ events in the next ninety minutes. In less than half a day, Turkey was hit by about one hundred and eighty earthquakes, two of which of magnitude larger than seven.

In (Baltzopoulos et al., 2023), the PGA of the horizontal recorded ground motions, available at AFAD, are compared with the mean (plus/minus one stan-
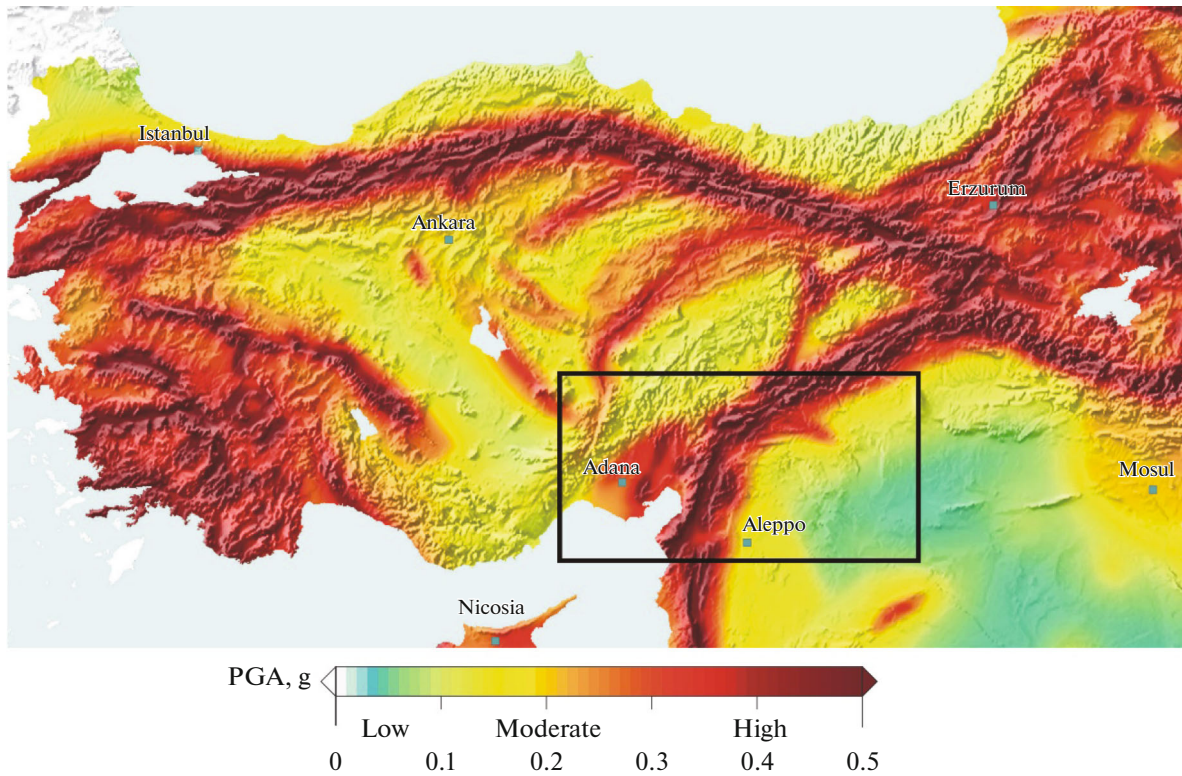
Fig. 1. A seismic zoning map of Turkey in terms of peak ground accelerations (PGA) for a return period of 475 years (Giardini et al., 2018). The rectangle frames the epicenter zones of the earthquakes.

dard deviation) of the ground motion prediction equation (GMPE) of (Bommer et al., 2012) developed for Europe and Middle East region. To allow such a comparison, the epicenter distance reported for each record is translated into the Joyner and Boore distance (R_{jb}) using the method after (Montaldo et al., 2005).

Figure 3, Fig. 4 and Fig. 5 from (Baltzopoulos et al., 2023) show the PGA recorded during the three earthquakes of February 6, 2023: the M7.8 main shock—at 4:17, M6.6—at 4:28, and M7.6—at 13:24 local time (UTC+3).

As seen from Fig. 3–Fig. 5, (1) no data are available for R_{jb} of less than 10 km, (2) within the mean distance range (from 10 to 100 km), the recorded data generally agree with the GMPE results, (3) the records obtained at $R_{jb} > 100$ km yield PGA below the values obtained from the selected GMPE.

Altogether, 274 records of the M7.8 event were obtained, of which—23 on rock, 46—on soft soil, and 103—on stiff soil; for the remaining 174, V_{s30} is unknown. 135 records of the M6.6 earthquake were obtained: 17—on rock, 19—on soft soil, 52—on stiff soil, and 47—in unknown soil conditions. 240 records of the M7.6 earthquake were obtained: 25—on rock, 38—on soft soil, 81—on stiff soil; for the other 96 V_{s30} is unknown.

Table 2 from (Baltzopoulos et al., 2023) reports data on 10 seismic stations that recorded the highest values of the PGA during the M7.8 earthquake: the station codes, their coordinates, the PGA for two horizontal and one vertical components, and their epicenter distances.

Table 1. Data about the three largest magnitude events in the earthquake sequence

Date	Time (UTC+3)	Magnitude	Long., °	Lat., °	Depth, km	Mechanism*
Feb. 6, 2023	04:17:36	7.8−7.7	37.08	37.17	20	Strike-Slip
Feb. 6, 2023	04:28:19	6.7−6.6	36.81	37.13	40	Strike-Slip
Feb. 6, 2023	13:24:49	7.5− 7.6	37.24	38.11	10	Strike-Slip

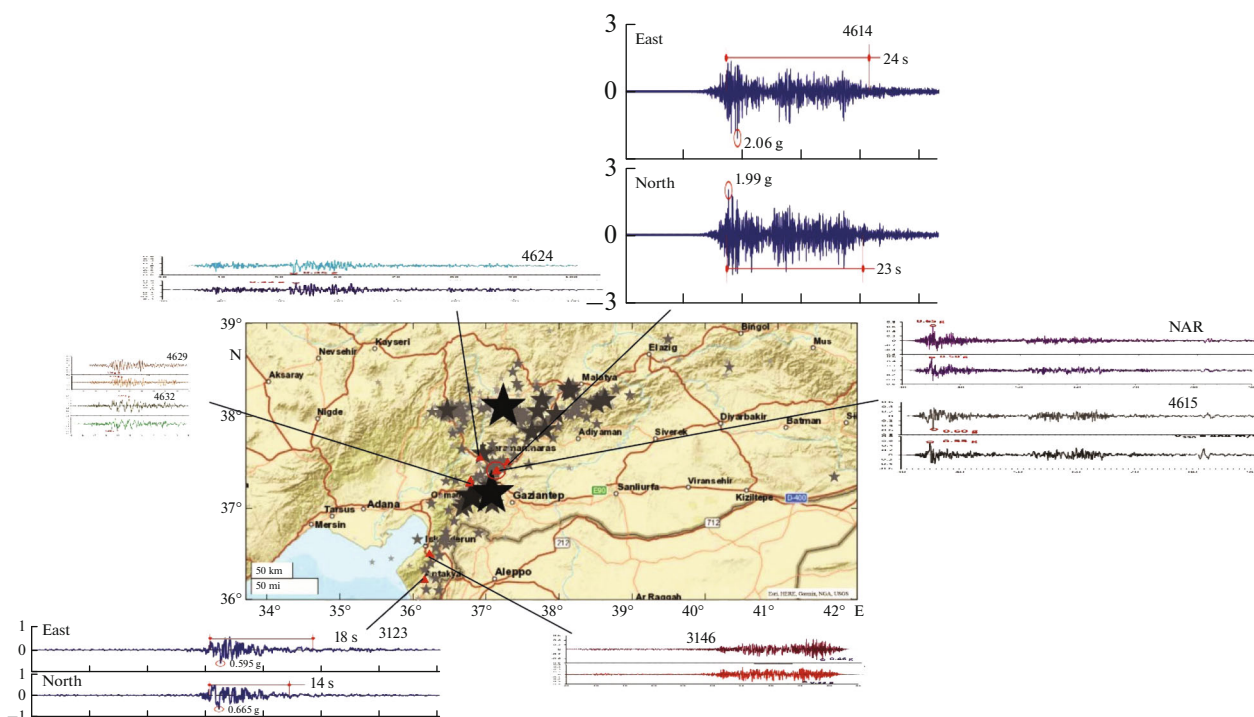* Based on fault models from literature (Gülerce et al., 2017).

Fig. 2. Epicenters of the M7.0+ events and aftershocks (black and grey starts) showing the fault plane of the main shock (after (Baltzopoulos et al., 2023)) and acceleration time histories from the stations closest to the epicenter of the M7.8 event (from (Baltzopoulos et al., 2023; Malhotra, 2023; Garini and Gazetas, 2023)).

Table 3 and Table 4 report data on 10 seismic stations closest to the epicenters of the M6.6 and M7.6 events.

In (Baltzopoulos et al., 2023), the authors computed the Arias intensity and acceleration response spectra (5% damping) for all the stations. The response spectra are maximum at 0−1 s at small epicenter distances (up to 20 km) and are within a wider range of 0−2 s at greater distances (up to 140 km); at long distances, also narrowband spectra can be encountered. From the response spectrum plots it can be seen that during all the three earthquakes, ground

motions challenging for structures were recorded: the spectral amplitudes were as large as 2.8 g (Baltzopoulos et al., 2023).

MANIFESTATIONS OF EFFECTS OF DIRECTIVITY OF SEISMIC RADIATION FROM THE SOURCES OF THE 2023 TURKEY EARTHQUAKES. PULSE-LIKE GROUND MOTIONS

The analysis of seismic records obtained during the Turkey earthquakes shows that sometimes, at great epicenter distances, no significant attenuation of the

Table 2. Data of the stations closest to the epicenter of the M7.8 event

| Station code	Longitude	Latitude	PGA_NS, cm/s^2	PGA_EW, cm/s^2	PGA_UD, cm/s^2	R_{epi}
4615	**37.14**	**37.39**	**587.70**	**556.41**	**664.56**	**18.23**
NAR	**37.16**	**37.39**	**646.52**	**578.79**	**398.66**	**19.48**
3144	36.49	36.76	611.28	763.43	451.65	73.56
3137	36.49	36.69	453.07	847.97	501.96	78.72
3145	36.41	36.65	600.06	696.45	663.17	87.50
3142	36.37	36.50	646.63	749.52	505.90	102.53
0201	38.27	37.76	474.07	879.99	318.99	121.71
3124	36.17	36.24	572.30	638.26	578.12	136.06
3123	36.16	36.21	655.35	593.89	867.60	138.94
3132	36.17	36.21	515.27	514.56	354.15	139.02
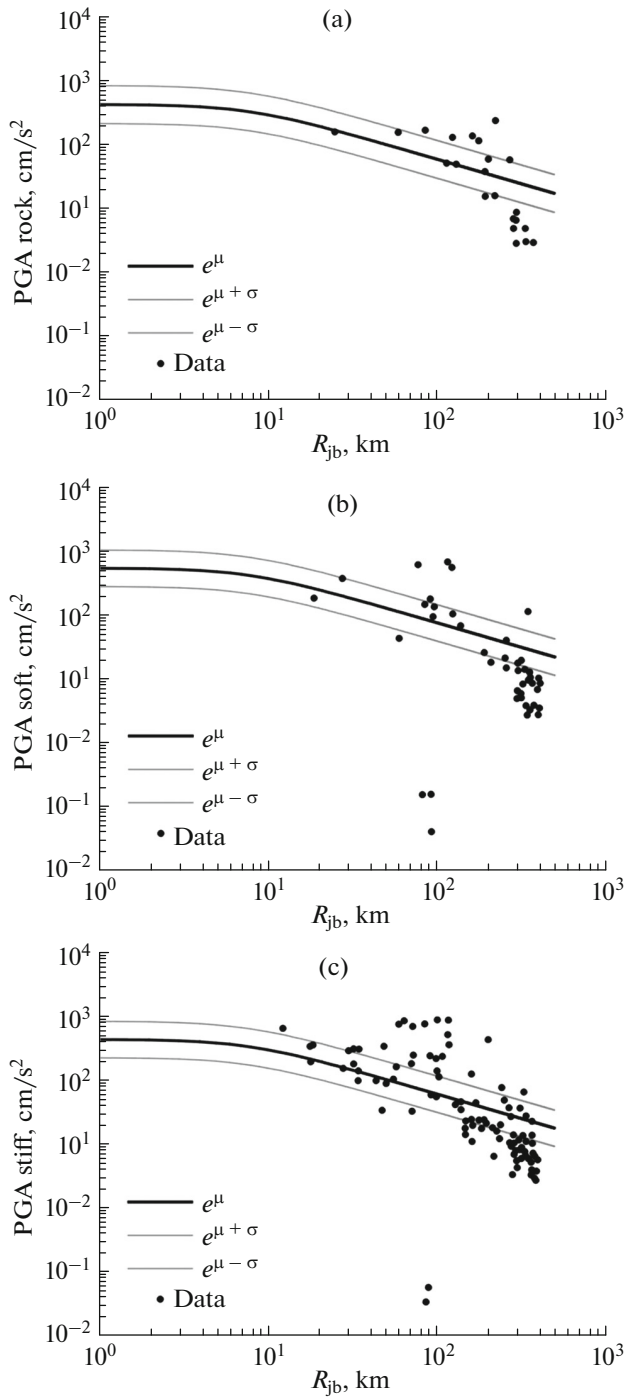
Fig. 3. PGA recorded during the $M7.8$ earthquake, and GMPE (Bommer et al., 2012): (a) for rock soil ($V_{s30} > 750$ m/s), (b) for soft soil ($V_{s30} \leq 360$ m/s), and (c) for stiff soil ($360 < V_{s30} \leq 750$ m/s).

Fig. 4. The same as in Fig. 3, for the $M6.6$ earthquake.

seismic vibrations is observed, apparently, due to the large dimensions of the fault zone, i.e. due to the effects of directivity of seismic radiation (Baltzopoulos et al., 2023).

Also, seismologists report heavy damages caused by the earthquakes: altogether, around 5000 buildings
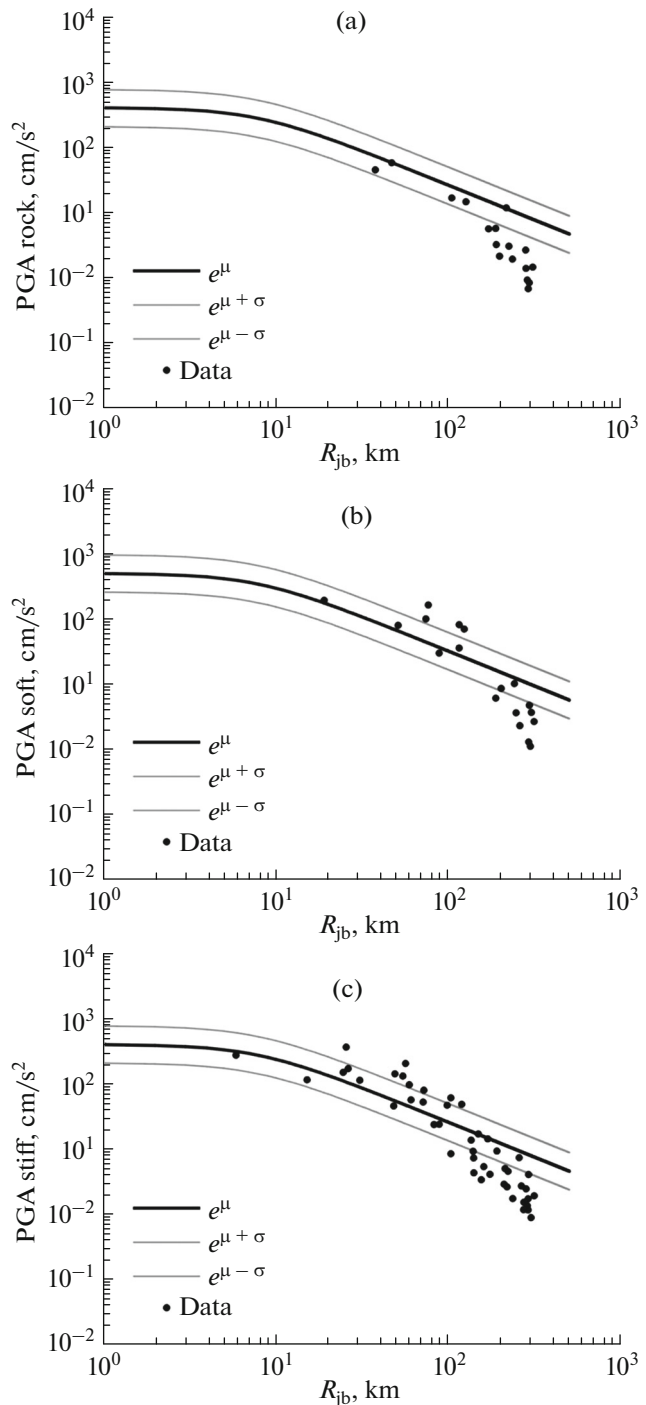
were destroyed in 10 provinces of Turkey; 10 big cities were seriously hit by the collapse of buildings.

Obviously, one of the causes of the destruction and collapse could be the observed so-called "pulse-like features."

It has long been observed that some near-fault earthquake ground motions are characterized by long-

duration acceleration pulses that correspond to unusually large velocity pulses. These pulses are the result of the earthquake rupture moving toward a given observation site (*forward propagation*). These pulses are typically much more pronounced on horizontal components oriented perpendicular to the fault. Directivity effects may occur at various source mechanisms, not only on strike-slip faulting but also on dip-slip faulting.

The study of theoretical dislocation models to understand the kinematics of near-field ground motions is by no means new (Anderson and Bertero, 1987). However, the topic has gained particular recognition after the 1994 Northridge earthquake and the 1995 Kobe earthquake. Based on the empirical analysis of near-fault records of strong motion and verification by means of broadband simulations, proposals have been made on the quantification of these effects to modify the existing empirical attenuation relationships in order to account for the average rupture directivity effects (Somerville et al., 1995) and for the forward rupture directivity effects (Abrahamson, 1998; Somerville et al., 1996).

Ground motions with a pulse at the beginning of the velocity time history are regarded by engineering seismologists as a special class of ground motions that cause severe damage to structures. This kind of pulse motions are usually observed on near-fault sites because such motions are caused mainly by the directivity effects of seismic radiation (Somerville et al., 1997; Somerville, 2003; 2005; Spudich and Chiou, 2008).

Pulse-like ground motions lead to amplification of the response spectra of engineering structures (usually, the narrowband, which makes the structure to behave inelastically at these frequencies), therefore, they are more challenging for structures than strong motions of non-pulse forms, at least, on average (Baez and Miranda, 2000; Iervolino et al., 2012; Shahi and Baker, 2011).

So, pulse-like ground motions impose severe demand on structures and are known to have already caused major damage during earthquakes in the past, as described, for example, in (Bertero et al., 1978; Anderson and Bertero, 1987; Hall et al., 1995; Iwan, 1997; Alavi and Krawinkler, 2001; Menun and Fu, 2002; Makris and Black, 2004; Mavroeidis et al., 2004; Akkar et al., 2005; Luco and Cornell, 2007).

The effect of pulse-like velocity time histories in the near-fault zones on the response of engineering structures was first pointed out by Mahin and Bertero during the 1971 San Fernando earthquake (Mahin et al., 1976; Bertero et al., 1977). After the 1979 Imperial Valley earthquake, Anderson and Bertero (Anderson and Bertero, 1987) identified the incremental velocity as an important parameter affecting the maximum inelastic response of structures subjected to strong ground motions in the near-fault zones.
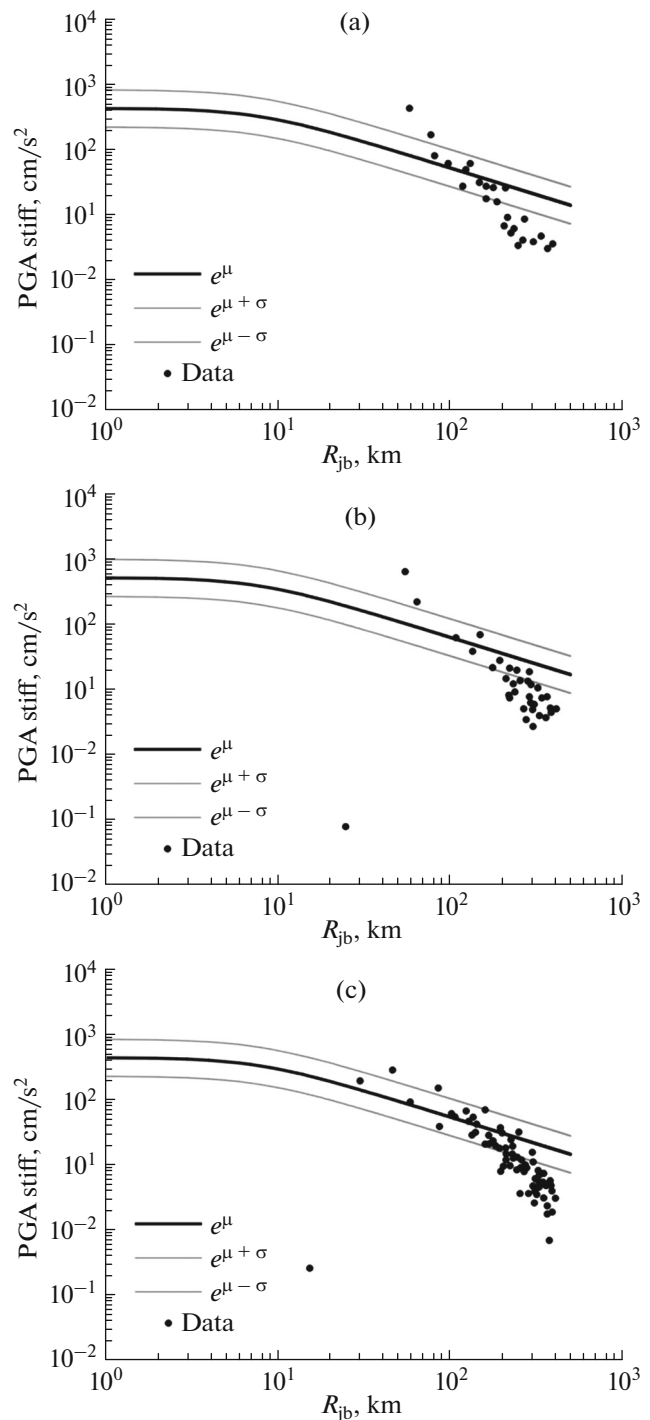

Fig. 5. The same as in Fig. 3, for the M7.6 earthquake.

After the 1994 Northridge and the 1995 Kobe earthquakes near-source factors have been introduced in the 1997 Uniform Building Code (UBC, 1997). These factors range from 1.0 to 2.0 depending on the source type and the closest distance to the known seismic source. However, these factors have been introduced based on limited data and studies and do not

Table 3. Data of the stations closest to the epicenter of the *M*6.6 event

Station code	Longitude	Latitude	PGA_NS, cm/s²	PGA_EW, cm/s²	PGA_UD, cm/s²	R_{epi}
4616	**36.84**	**37.38**	**233.01**	**259.80**	**145.89**	**10.74**
2712	36.73	37.18	445.29	336.80	319.34	21.27
NAR	37.16	37.39	61.86	137.37	55.95	23.15
4624	36.92	37.54	146.37	182.10	79.52	25.81
4617	36.83	37.59	116.28	147.62	33.94	32.29
2708	**36.65**	**37.10**	**312.95**	**355.45**	**208.24**	**33.12**
8002	36.56	37.19	127.15	163.64	125.62	34.07
2718	**36.63**	**37.01**	**220.03**	**308.99**	**129.75**	**41.97**
2716	36.69	36.86	86.90	179.51	72.34	53.84
3143	36.56	36.85	113.80	136.46	75.55	59.98

Table 4. Data of the stations closest to the epicenter of the *M*7.6 event

Station code	Longitude	Latitude	PGA_NS, cm/s²	PGA_EW, cm/s²	PGA_UD, cm/s²	R_{epi}
4408	37.89	38.10	52.37	142.29	275.29	56.74
4409	37.49	38.56	214.22	150.23	62.29	56.86
4612	**36.48**	**38.02**	**637.92**	**522.63**	**372.97**	**66.68**
4406	37.97	38.34	428.25	373.32	286.23	70.17
3802	36.50	38.48	193.76	218.62	118.06	77.41
0129	36.21	38.26	149.67	166.27	80.81	91.84
4405	37.94	38.81	136.82	149.87	83.11	100.81
0141	35.53	37.56	78.64	189.25	74.48	161.28

explicitly take into account the difference between the effects of near-fault ground motions on elastic and on inelastic structural response. Other design recommendations have introduced factors that explicitly take into account the demands to maximum inelastic and maximum elastic lateral displacements (ATC, 1996; FEMA, 1997). These factors permit the estimation of maximum inelastic displacements using the results of linear elastic analyses.

As stated above, the best-known causes of the appearance of pulse-like features of ground motion are the effects observed near the source, such as rupture directivity or thrust. In segments along the rupture propagation direction, an almost simultaneous arrival of S waves radiated by the propagating crack at different points of the rupture plane can be observed. These are the so-called directivity effects that manifest themselves in ground motion velocity time histories, when constructive interference of waves can cause noticeable double-side pulses (Somerville et al., 1997).

In (Baltzopoulos et al., 2023), the seismic records obtained near the fault planes of the three large earthquakes in Turkey were analyzed for the presence of the pulse-like features. At the preliminary stage of the analysis, due to the lack of sufficient information on the fault geometry and fault slips, the analysis is limited to characterization of certain near-source records as pulse-like based on the features of the waveforms, without considering the rupture process depending on the recording site's location.

Ten records from each of the three earthquakes were included in the investigation (Table 2–Table 4), for a total of thirty. Velocity time histories were obtained via integration of the accelerograms on horizontal components; the resulting vector was studied by being rotated over more than one hundred and eighty degrees at a step of one degree. For each orientation, a consolidated wavelet-based algorithm was applied to identify candidate pulse signals in the velocity time histories (Baker, 2007), and a pulse indicator (*PI*) was estimated. Ground motions were preliminarily characterized as pulse-like, if they exhibited a consistently high score of *PI* > 0.90 over an arc of more than 60°, and also a satisfactory match of the pseudo-velocity spectra of the ground motion and the candidate pulse wavelet, around the pulse period T_p (Baltzopoulos et al., 2020).
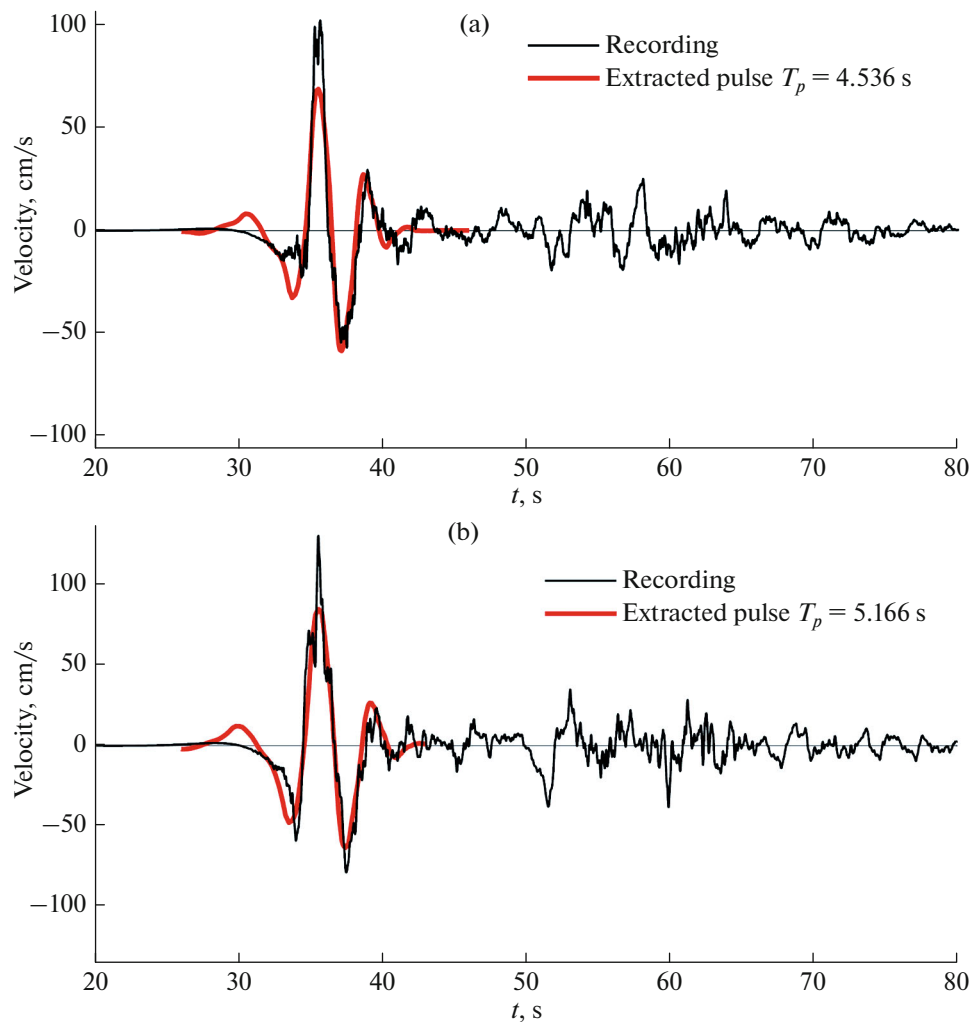
Fig. 6. Identified pulse-like velocity time histories at the stations NAR (a) and 4615 (b) (from (Baltzopoulos et al., 2023)).

As a result, six of thirty investigated records were characterized as pulse-like (Fig. 6); they are given in bold in Table 2—Table 4. These are the records of the main shock $M7.8$ from stations NAR and 4615, the record of the $M7.6$ event from station 4612, and the records of the $M6.6$ event from stations 2708, 2718 and 4616. The periods of all identified pulses are somewhat below the median predictions considering the values obtained from regression models. For example, one such model would predict the median T_p of 7.5, 6.7 and 2.4 s for M_w 7.8, 7.6 and 6.6, respectively (Baltzopoulos et al., 2023).

EARLY TRANSITION TO A SUPERSHEAR RUPTURE PROPAGATION IN THE SOURCE OF THE $M7.8$ KAHRAMANMARAS EARTHQUAKE (ROSAKIS ET AL., 2023)

Preliminary models of the development of slips in the source of the $M7.8$ earthquake of February 6, 2023, based on teleseismic data as well as on multiple inversions, suggest that the rupture initiated at 4:17:355 local time on a splay branch fault in the near proximity of the East Anatolian Fault. The precise location of the hypocenter is currently uncertain. The preliminary hypocenter location was estimated by AFAD to be 37.288° N 37.042° E, with a depth of ~8 km. According to the United States Geological Survey (USGS), the hypocenter coordinates were 37.166° N 37.042° E ± 6.3 km (indicated by the red star in Fig. 7) with a depth of ~18.3 km.

The rupture propagated north-east, then moved to the East Anatolian Fault and initiated a sequence of seismic events. Subsequent geodetic inversions confirmed the multi-segment nature of the $M7.8$ rupture. The earthquakes caused catastrophic destructions and substantial humanitarian and financial losses.

The scale of the event and the total rupture length appeared to be much larger than could be expected based on the analysis of historical records and the current tectonic situation in the south of Turkey (Acarel
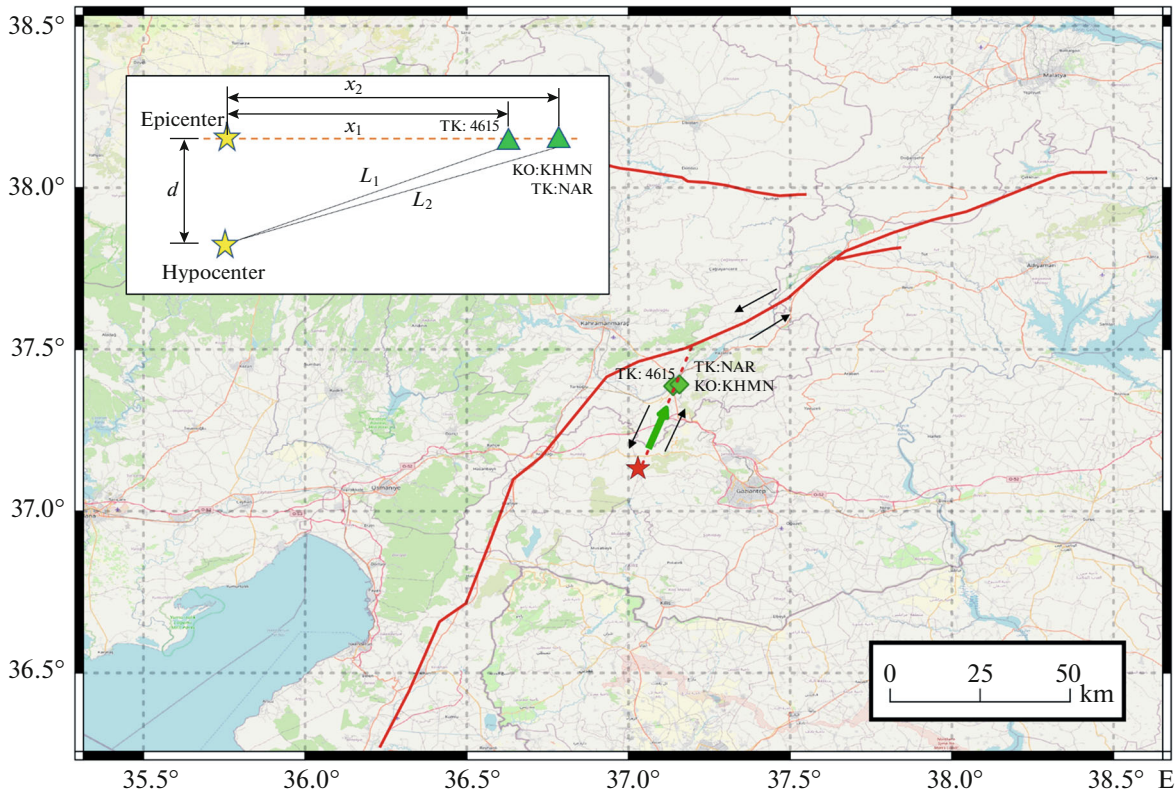
Fig. 7. The East Anatolian Fault (EAF) zone, the estimated location of the hypocenter (the red star) of the M_w 7.8 earthquake. The dashed line represents the inferred splay fault trace according to AFAD records. The green diamonds indicate the locations of the nearest seismic stations to the fault trace. The black arrows indicate the sense of motion of the fault. The insert is a schematic of the locations of the stations (from (Rosakis et al., 2023)).

et al., 2019): the magnitude of the largest earthquake on the East Anatolian Fault for the last several hundred years was 7.2. This, together with the intensity of the measured strong shaking, motivated a group of US researchers A. Rosakis, M. Abdelmeguid, and A. Elbanna (Rosakis et al., 2023) to investigate the nature of the rupture initiation, propagation, and the possibility of its early supershear transition.

Figure 7 illustrates the estimated location of the hypocenter, the direction of the splay fault, which, judging by the aftershocks, was striking at ~22°, and the direction of motion: left lateral for both the splay fault and the East Anatolian Fault. Three stations are located close to the splay fault (Fig. 7): two of them, TK:NAR and KO:KHMN, are located at one site at 37.3919° N 37.1574° E; they are twin stations. The third station, TK:4615, is located closer to the epicenter, at 37.386° N 37.138° E. Records from the three stations provide an insight into the near-field characteristics of the rupture on the splay fault; these records are unique observations (Rosakis et al., 2023).

Figure 8a shows velocity time histories of the M7.8 earthquake from the twin stations TK:NAR and KO:KHMN along the fault parallel, the fault normal and the vertical directions. The stations use various

instruments, and the good agreement between the records provides confidence in the quality of data.

The velocity time histories from the twin stations reveal unique characteristics: (1) the FP component is more dominant than the FN component, which is atypical of sub-Rayleigh ruptures that feature more dominant fault normal versus fault parallel components. The dominant fault parallel component is a characteristic feature of supershear ruptures (Rosakis et al., 1999), in which the rupture propagation speed exceeds the shear wave speed. Such a behaviour has been observed both in the laboratory (Mello et al., 2014; 2016), and in the field (Mello et al., 2014; Dunham and Archuleta, 2004; Bouchon et al., 2001; Zeng et al., 2022), and has also been predicted by the theory (Mello et al., 2014; Dunham and Archuleta, 2004; Dunham and Bhat, 2008). This provides evidence for supershear rupture propagation towards the twin stations.

We observe intense motion associated with the arrival of the Mach cone at the station. By measuring the ground motion associated with the Mach front, we find that the ratio of the fault parallel particle velocity component to the fault normal component is ~1.2. As discussed by Mello et al. (2016), these changes are due to the arrival of the shear Mach fronts. As theoretically
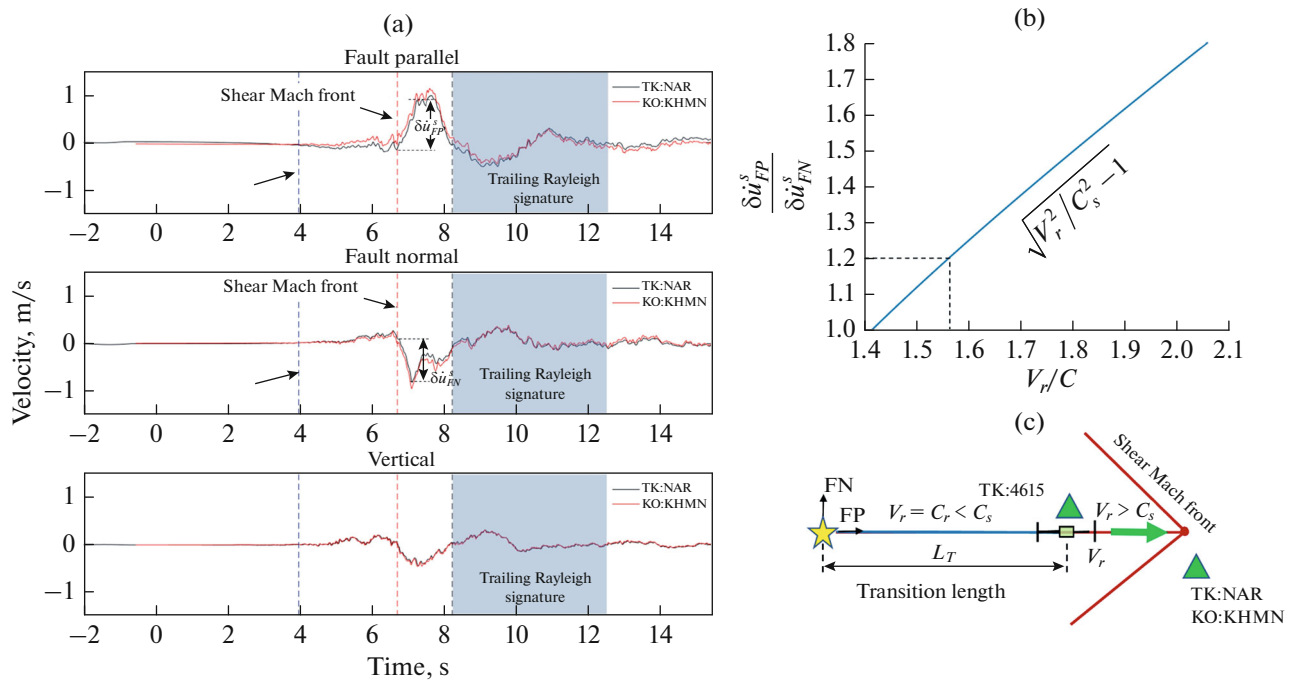
Fig. 8. Near-field records at the stations TK:NAR and KO:KHMN, indicating the supershear rupture propagation: (a) time histories (instrument corrected) of the fault parallel, fault normal and vertical velocities recorded at the stations TK:NAR (the black line) and KO:KHMN (the red line). The blue dashed line indicates the arrival of *P*-waves, the red dashed line indicates the arrival of the shear Mach front, and the black dashed line indicates the arrival of the trailing sub-Rayleigh signature; (b) the theoretical relationship between the ratios of FP and FN velocity changes due to the passage of the Mach front and the supershear rupture speed normalized by the shear wave speed; (c) a schematic diagram showing the top view, locations of the stations (green triangles) and the shear Mach front. The epicenter is marked by a yellow star. The transition point is marked by the green square and associated error bars. The green arrow indicates the rupture propagation direction (from (Rosakis et al., 2023)).

shown in (Mello et al., 2016), the ratios of particle velocities depend uniquely on the ratio of the rupture propagation speed and the shear wave speed as follows $\sqrt{(V_r/V_s)^2 - 1}$. This relationship is shown schematically in Fig. 8b. Accordingly, for a ratio of ~1.2 the supershear rupture speed is ~$1.5V_s$. The black dashed line in Fig. 8a indicates the return to the sub-Rayleigh rupture speed, at which the rupture propagated before it transitioned to supershear. The top view (Fig. 8c) shows the location of the three stations relative to the epicenter, the length of the transition, after which the rupture propagation speed exceeds the shear wave speed, and the Mach cone passage through the twin stations.

Figure 9a shows the velocity time histories obtained from the station TK:4615 along the fault parallel, the fault normal and the vertical directions (AFAD data). These records are qualitatively different from the records shown in Fig. 8a. Indeed, here the normal velocity component is larger than the parallel component, which is characteristic of a primarily sub-Rayleigh rupture propagation. However, a detailed examination of the fault parallel velocity time history indicates the presence of a small but well-defined

pulse before the transition to the sub-Rayleigh wave speed (the shaded area in Fig. 9a).

Rosakis et al. (2023) believe that this feature is a supershear pulse, which has just been formed ahead of the rupture that is still propagating at the sub-Rayleigh wave speed. The authors hypothesize that the station TK:4615 is located very close to the point, where the rupture transitioned from sub-Rayleigh to supershear. It should be noted that the probability of capturing the early stages of the sub-Rayleigh to supershear rupture transition is very low, and has never been observed before in near-fault records. However, this transition has been reported experimentally in laboratory earthquake simulations (Xia et al., 2004; Mello et al., 2016). Specifically, Mello et al. (2016) captured this transition by comparing dynamic photo images of the initial stages of the formation of the supershear pulse with the near-fault velocity time histories. The velocity time histories were obtained by a pair of laser velocimeters recording the fault parallel and the fault normal components (Mello et al., 2016).

To investigate the validity of the hypothesis on the supershear rupture transition, Rosakis et al. (2023) performed computations: the authors assumed $V_s = 3320$ m/s and $V_p = 5780$ m/s, which is in a good agreement with the velocity models for the southern Turkey region
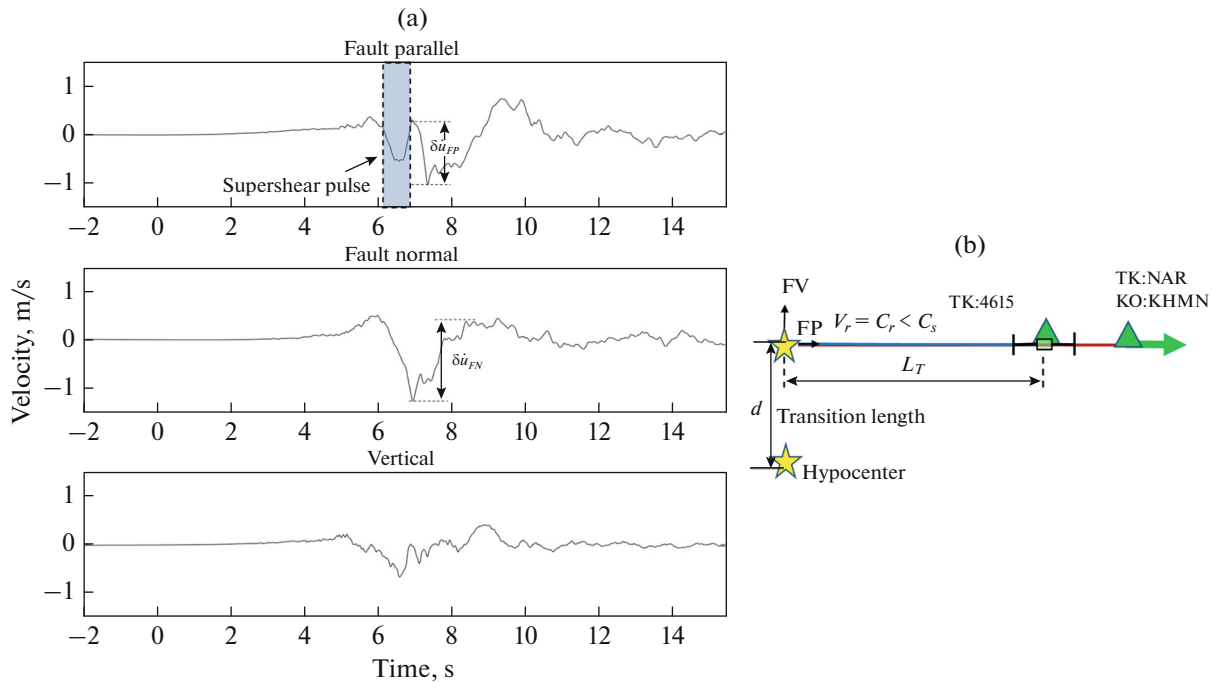
Fig. 9. The transition from sub-Rayleigh to supershear rupture propagation is captured by the station TK:4615: (a) time histories of the fault parallel, fault normal and vertical velocities. The highlighted region indicates the emergence of a supershear pulse ahead of a sub-Rayleigh rupture; (b) a schematic of the location of the stations (green triangles) relative to the epicenter and the hypocenter (yellow stars). The transition point is marked by the green square and associated error bars. The green arrow indicates the rupture propagation direction. The station TK:4615 is located within close proximity to the transition point (from (Rosakis et al., 2023)).

(Acarel et al., 2019). Then, the Rayleigh wave speed is $V_R = 3050$ m/s, and the rupture propagation speed is $V_r = 4960$ m/s. Based on the P-wave arrival time to the twin stations and using the velocity estimates given above, for the hypocentral depth of 10.9 km we obtain the length of transition of ~19.45 km. Using the P-wave arrival time to TK:4615 station, we obtain the epicentral distance of the station TK:4615 of 19.15 km. So, for the 10.9 km hypocentral depth, we find that the location of the station TK:4615 coincides with the location of the sub-Rayleigh to supershear transition, which is consistent with the hypothesis. The estimate of the depth at 10.9 km is within the range predicted by the different agencies, AFAD and USGS. Furthermore, the distance between the twin stations and TK:4615 is estimated at ~1.6 km along the rupture propagation direction. Since the distance between the twin stations and TK:4615 is 2 km, this estimated difference in the epicenter distances is a plausible estimate.

Hence, the analysis of the three near-field velocity time histories of the M7.8 Kahramanmaraş earthquake shows that the rupture that propagated on the splay fault had transitioned from the sub-Rayleigh speed to the supershear speed (exceeding the speed of S-waves) at an epicenter distance of approximately 19.45 km. The near-field records also captured, for the first time, the in situ transition mechanism from sub-Rayleigh to supershear propagation and provided a picture of the near-fault particle motions in both the fault parallel and fault normal directions.

Since Mach fronts attenuate only weakly with distance, this early supershear transition on the splay fault may have enabled strong dynamic stress transfer to the nearby East Anatolian Fault and contributed to the continued rupture propagation that triggered a slip both in the North East and South West directions.

Indeed, prior studies have suggested that supershear ruptures are more effective in jumping across fault stepovers (Harris and Day, 1993) and activation of nearby faults (Templeton et al., 2009; Rousseau and Rosakis, 2009; Bhat et al., 2004). The early supershear transition on the splay fault may have been favoured by the regional stress state. Seismological studies (Kartal et al., 2013) have suggested that the splay fault existed in a N16.4° E compression and N80.8° W extension regime. So, the splay fault N22° E strike appears to be close to being perpendicular to the minimum stress, which reduces the overall normal stress on the fault. This may significantly reduce the fault strength parameter S (for example, $S < 1$) (Xia et al., 2004; Andrews, 1976) and favours the transition to supershear rupture over shorter distances. Rosakis et al. (2023) hope that further studies of the regional stress field and strong ground motion records will reveal more details about the nature of this complex multi-
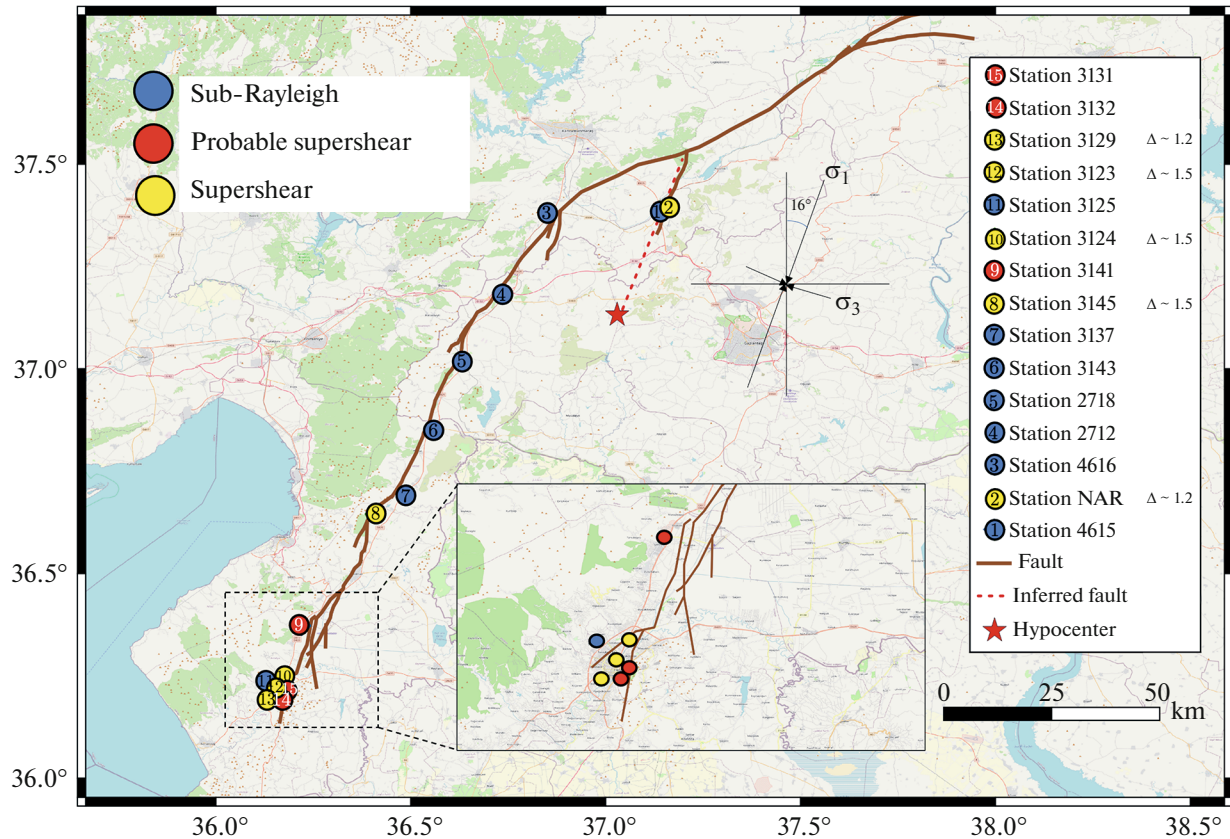
Fig. 10. A map of the East Anatolian Fault (EAF) zone highlighting the estimated location of the hypocenter of the M7.8 earthquake and the location of the stations (circles), distinguished by their colours, according to a ground record characteristic consistent with sub-Rayleigh (blue), supershear (yellow), and probable supershear (red). For stations that demonstrate supershear characteristics, the ratio of the fault parallel particle velocity to the fault normal component is indicated. The figure shows also a zoomed view of the location of the stations at the southern end of the trace according to USGS data (from (Abdelmeguid et al., 2023)).

segment rupture that led to such a large-scale human tragedy.

In their new study, Abdelmeguid et al. (2023) build a two-dimensional dynamic model of the rupture of the Kahramanmaraş earthquake on the basis of ground motion records, field studies of the tectonic situation and geometric features of the fault trace, through which they offer physical arguments to better constrain the rupture velocity profile for competing kinematic inversions and provide an insight into the mechanisms that contributed to devastation and humanitarian loss during the earthquake.

Similar to Rosakis et al. (2023), the authors investigate the ground motion velocity records along the fault parallel and the fault normal directions but expand their analysis to include all the near-field stations with complete and reliable records. The stations are classified based on the FP to FN ratio (Fig. 10).

The ground motion records reveal three locations in which the rupture propagation speed exceeded the S wave speed V_s. The first incident discovered in (Rosakis et al., 2023), was on the Narlı fault in very

close proximity to the hypocenter. After transitioning to the East Anatolian Fault, the rupture propagated bilaterally: one tip propagated north towards Malatya, the other tip propagated south–south-west towards Antakya.

Along the southern segment there are several stations that evidence the rupture speed in that direction. Specifically, the records at the stations 2712, 3143, and 3137 show larger FN components compared to the FP components, which suggests the sub-Rayleigh propagation speed along that EAF segment. The station 3145 shows an opposite (i.e. dominant) FP component: the FP to FN ratio at that station is approximately 1.5, which suggests that the rupture was propagating at a supershear speed. The location of the station 3141 on the fault bend (Fig. 10) indicates that the sudden change in the fault strike and the resulting change in the local stress state could have contributed to the transition to a supershear rupture.

Furthermore, we observe that the rupture transitioned again to supershear near the southern end of the fault trace, as indicated by the multitude of sta-
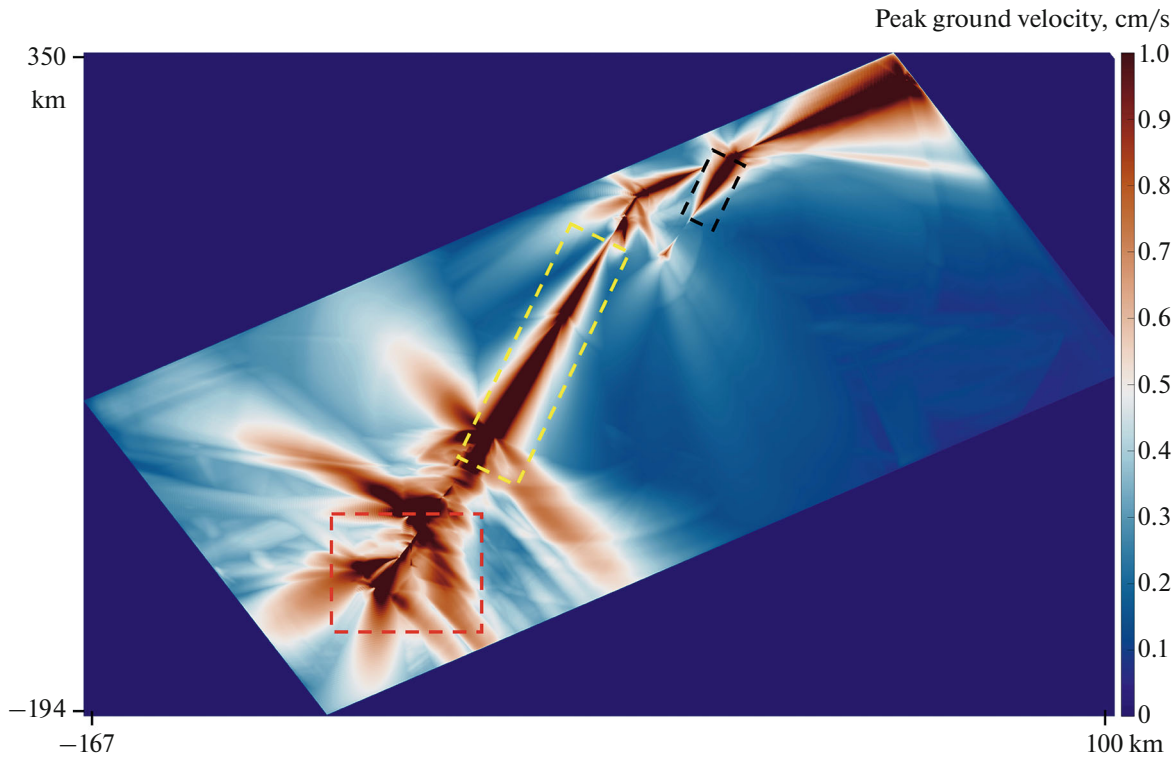
Fig. 11. Peak ground velocity (PGV) distribution obtained from the numerical simulation of dynamic rupture (from (Abdelmeguid et al., 2023)).

tions. Except for the station 3125, the other records indicate a dominant FP to FN ratio; however, the ratio varies between the stations. This can be explained by the complexity of the fault network: the multiple kinks and branching segments in the southern tip suggest a complex stress state that contributes to bursts of supershear on some segments and complex waveforms that may obscure the Mach cone signature in other locations.

The analysis of the near-field station records suggests that the rupture propagated over the Narlı fault as well as the southern segment at speeds below the Rayleigh and supershear speeds. Due to the sparsity of the stations around the junction point of the Narlı fault with the EAF, as well as along the northern EAF segment, we do not have enough information to estimate the rupture propagation speed.

To fill this gap, the authors built a dynamic rupture model, having computed the strength parameter S, characteristics of friction and the stress state in the region. Templeton et al. (2009) studied a wide spectrum of branch angles and showed that for acute branching angles $\sim 32°-35°$, similar to the angle between the Narlı fault and the EAF, the crack speed along the branch would be initially the same or slightly smaller than its propagation speed prior to encountering the branch.

The constructed dynamic rupture model that reflects the above key characteristics of the complex $M_w 7.8$, event provides peak velocity estimates presented in Fig. 11.

The distribution of the peak ground velocities (PGV) in the near-fault zones demonstrates high PGV values. Geometrical complexity, triggering of segmented faults and largely unattenuated shock fronts due to the supershear crack propagation favour wider spreading of strong ground motions.

Parameters of strong ground motions correlate with ground failure estimates. The landslide distribution maps are generated based on the spatially distributed estimates of PGV, topographic slope, lithology, land cover type, and a topographic index designed to estimate variability in soil humidity. The landslide distribution models estimated by USGS are consistent with the co-seismic landslides caused by the 2023 Turkey earthquakes. The liquefaction models are based on S wave velocity in the upper 30 m V_{S30}, modelled water table depth, distance to coast, distance to river, distance to the closest water reservoir, precipitation and PGV. The liquefaction estimates from USGS agree with the liquefaction sites based on remote sensing data (Taftsoglou et al., 2023). Based on both the preliminary reports and USGS estimates, we observe that regions with more intense ground motion obtained from the dynamic rupture model (Fig. 11) are consis-

tent with regions of substantially larger ground failure. Certainly, failure distribution can be also influenced by phenomena such as wave amplification in ground layers and sedimentary basins, and, of course, by the type and quality of civil engineering.

Records of strong motions show us a relatively narrow (1−2 s) dominant pulse in the regions with supershear crack propagation, such as observed in Antakya compared to records corresponding to the sub-Rayleigh crack propagation.

The presence of a relatively narrow velocity pulse imposes higher demands on the structures, increasing the possibility of structural collapse. Specifically, in the dynamic rupture model we observe supershear propagation at the southern end of the fault segment near Antakya, resulting in high particle velocity ($\approx$2 m/s) and widespread ground shaking (red dashed box). Simultaneously, the records highlight significant ground failures associated with both liquefaction and co-seismic landslides within the same region. A similar pattern is observed in several directions northwards, toward Malatya, where we see a correlation of the supershear crack propagation with widespread landslides. The predicted liquefaction zone at the northern end of the Narlı fault (black dashed box) also seems to correlate well with the region of transition and supershear propagation on that segment.

So, the analysis of near-field records of the M7.8 Kahramanmaraş earthquake reveals (Abdelmeguid et al., 2023) that the rupture propagation speed was spatially not uniform, varying from sub-Rayleigh to supershear (exceeding V_s). This is consistent with experimental studies and numerical simulations of geometrically complex faults, which demonstrated that the existence of kinks and branches may have significant implications on the rupture speed depending on the geometrical setup in relation to the orientation of the main fault. The geometrical complexity of the fault contributed to the emergence of transient supershear ruptures.

A combination of high stress drop on the Narlı fault and high stresses on the East Anatolian Fault at the point of their junction contributed to the continued rupture propagation. Had the stress field orientation been different by a few degrees, the overall size of the earthquake could have been much smaller.

When a rupture transitions from sub-Rayleigh to supershear propagation, there still is a sub-Rayleigh signature following the leading supershear rupture. As a consequence, a building at a near fault location will first experience an intense shaking due to the shock waves of the leading supershear rupture front.

This part of the shaking will occur very rapidly (narrow velocity pulses) and is characterized by the fault parallel component of the ground velocity being larger than the fault normal component. For instance, such enormous differences in the peak ground velocities PGV$_{FP}$ and PGV$_{FN}$ ($\approx$2 times) are observed at the station 3129 in Antakya, where the city was actually destroyed. However, soon (seconds later) after that, the building will experience shaking of a different type, which is associated with the passage of the trailing Rayleigh rupture. This shaking features a dominant fault normal component. The double punch effect associated with the first (leading) arrival of the shock front and then the subsequent (trailing) Rayleigh signature can have a devastating impact on the structure. Such effects of supershear ruptures on soils and structures require further investigations. The role of physics-based dynamic modelling is crucial in the understanding of the mechanism that lead to such a devastating outcome. While we cannot currently predict the occurrences of earthquakes, we may use this evidence to predict the response of soils and structures during future earthquakes.

ACCOUNTING FOR DIRECTIVITY EFFECTS IN PROBABILISTIC SEISMIC HAZARD ANALYSIS (PSHA)

Directivity effects imply manifestation of the phenomenon of the interference of waves radiated from multiple fault surface points in case of a simultaneous rupturing during the propagation of the rupture front at speeds close to the propagation velocity of S waves. As a result of the propagation of the rupture in the direction to an observation site at a speed close to S wave propagation velocity, the greater part of the energy radiated in the source arrives at the site as a powerful pulse. The so-called pulse-like features occur—velocity time histories of a special shape with a strong pulse at the beginning of the record (Fig. 12).

Directivity effects manifest themselves in the amplification of ground motions at points located in the direction of rupture propagation and they are determined by the geometrical dimensions of the fault, the location of the crack nucleation point and the speed of its propagation, the location of the observation site relative to the fault, and the frequency content of the interfering waves. Ground motions intensified by the directivity effects can be extremely devastating (Mavroeidis and Papageorgiou, 2003; Kalkan and Kunnath, 2006).

One of the first models to account for directivity effects in ground motion prediction equations (GMPE) was suggested in (Somerville et al., 1997). The authors individually analyzed dip-slip and strike-slip faults. It was assumed that ground motion amplitude variations in the near-fault zones depend on two parameters: (1) the angle between the crack propagation direction and the direction of the propagation of waves from the source to the observation site (φ for the first type of slip, θ—for the second type of slip); (2) the fraction of the width d (for the first type of slip) or the length s (for the second type of slip) of the rupture surface that lies between the hypocenter and the observation site. Respective directivity parameters for the two
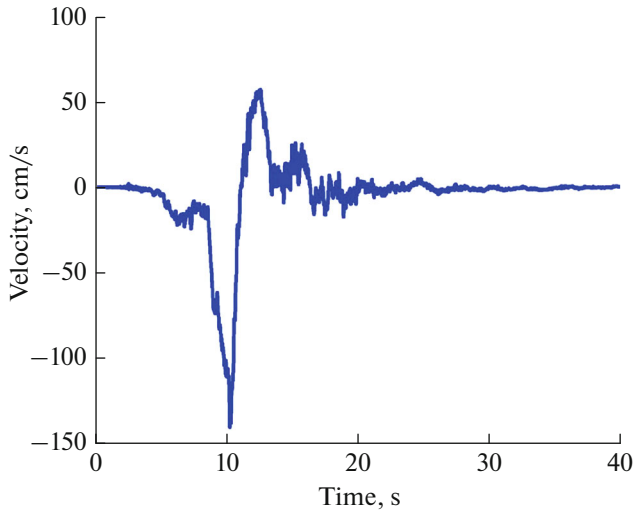
Fig. 12. The fault normal component from the velocity time history of the 1992 Landers earthquake (from (Tothong et al., 2007)).

types of slips are given by: $X = \left(\dfrac{s}{L}\right)\cos\theta$, $Y = \left(\dfrac{d}{W}\right)\cos\varphi$, where L and W are the fault plane length and width, respectively. Then, the corrections to the acceleration response spectrum amplitude estimates will be given by:

$$y = C_1 + C_2 X, \quad y = C_1 + C_2 Y,$$

where C_1 and C_2 are frequency-dependent regression coefficients.

It is important to note that the model implied that in case of strike slip the crack propagates in the strike-parallel direction only, and in case of dip slip—along the dip only. Furthermore, the model did not allow the estimation of directivity effects at points located around dipping faults, where the so-called neutral zone was introduced.

To overcome these limitations, Abrahamson (2000) suggested a modification of the model to constrain the values of the directivity parameters X and Y to 0.4, and Rowshandel (2006) generalized the model to include heterogeneous multidirectional ruptures and extend in this way the model applicability.

Spudich and Chiou (2008) suggested an analytical model of directivity effects based on the so-called isochrone directivity predictor (*IDP*):

$$IDP = CSR_{ri},$$

$C = \dfrac{\min(\tilde{c}', 2.45) - 0.8}{(2.45 - 0.8)}$—the normalized isochrone velocity ratio:

$$\tilde{c}' = \left(\frac{\beta}{v_r} - \frac{(R_{HYP} - R_{RUP})}{D}\right)^{-1}, \text{ at } D > 0, \; \tilde{c}' = \frac{v_r}{\beta}, \text{ at } D = 0,$$

where v_r—the rupture velocity, β—the shear wave speed in the medium , R_{HYP} and R_{RUP}—the hypocentral distance and the shortest distance from the rupture surface to the observation site x_s, D—the distance from the hypocenter x_h to the rupture surface point closest to the observation site x_c.

$$S = \ln[\min(75, \max(s, h))],$$

where s—the distance from the hypocenter x_h to the point x_c measured along the fault strike, h—the distance from the upper rupture edge to the hypocenter, measured along the fault dip.

$$R_{ri} = \max\left(\sqrt{R_u^2 + R_t^2}, \varepsilon\right)$$—the scalar amplitude of the radiation pattern,

where R_t and R_u—the strike-normal and the strike-parallel components of the radiation pattern, $\varepsilon = 0.2$.

The final directivity effect model is given by:

$$f_D = f_R(R_{RUP}) f_M(M)[a + bIDP],$$

where $f_R(R_{RUP}) = \max\left[0, \left(1 - \dfrac{\max(0, R_{RUP} - 40)}{30}\right)\right]$ takes the value 1 for $0 \le R_{RUP} \le 40$ and tapers linearly to 0 at $R_{RUP} \ge 70$, $f_M(M) = \min\left[1, \dfrac{\max(0, M - 5.6)}{0.4}\right]$ takes the value 0 at $0 \le M \le 5.6$ and rises linearly to 1 at $M \ge 6.0$, a and b—the frequency-dependent regression coefficients.

Comparing the isochrone predictor model with the models by Somerville et al. (1997) and Abrahamson (2000), the authors note that the model-predicted ground motion amplification and deamplification resemble in general the estimates obtained from the Abrahamson (2000) model, and are almost twice as low as the estimates from the Somerville et al. (1997) model for all spectral periods.

In the models described above, the influence of directivity effects is manifested in monotonic amplification or attenuation of the amplitudes of the acceleration response spectrum in a wide range of spectral periods, that is why such models are sometimes referred to as broadband models. On the other hand, some authors (for example, Somerville, 2005; Tothong et al., 2007; Iervolino et al., 2012)) point out that according to the available observational data, directivity effects occur in a narrow range of spectral periods that is close to the period of the waveform pulse (T_p), and such models are called narrowband models.

Developing the approach proposed in (Tothong et al., 2007), Shahi and Baker (2011) suggested a com-

prehensive framework to incorporate the effects of pulse-like features in probabilistic seismic hazard analysis (PSHA). The framework uses the pulse-like feature identification algorithm (Baker, 2007) that eliminates the ambiguity of the interpretation of data in the course of visual analyses of earthquake records. Among other important elements of the framework are: the model of the probability of the occurrence of pulse-like ground motions at the observation site depending on the location relative to the earthquake source, the model of the probability of the occurrence of pulse-like ground motions at a specific orientation, the model of dependence of the pulse period on the earthquake magnitude, and the model of the amplification of the acceleration response spectrum components depending on the pulse period.

The listed models were calibrated on a subset of pulse-like features from the Next Generation Attenuation (NGA) Project database, identified with the use of the algorithm by Baker (2007). To demonstrate the application of the framework, seismic hazard maps were computed in the units of spectral accelerations at the 5 s period for a strike-slip fault using the proposed framework and using the conventional PSHA. Based on the results, a seismic hazard amplification map was computed relative to the conventional PSHA for a near-fault zone. For comparison, a similar hazard amplification map was computed on the basis of the Abrahamson (2000) model. Both maps yielded close seismic hazard amplification values, with the amplifications obtained using the described framework being concentrated in a much narrower area around the fault than the amplifications obtained using the Abrahamson (2000) model. Significant differences are, probably, due to the update of the directivity effect model thanks to a substantially extended database accumulated after the publications (Somerville et al., 1997; Abrahamson, 2000).

In (Spanguolo et al., 2016), the directivity effect model from (Spudich and Chiou, 2008) was used to build maps of seismic hazard in and around Istanbul. The seismic hazard in that region is due to the proximity of two North Anatolian Fault segments lying under the Sea of Marmara at around 20 km from Istanbul. The location of the hypocenter on the fault segments was modelled using random values with a normal distribution, a uniform distribution, and a distribution determined on the basis of crack propagation simulations. The results of the analysis showed that accounting for directivity effects significantly increases PSHA estimates (up to 25% for seismic hazard with a return period of 475 years) expressed in the units of spectral accelerations at the 2 s period.

The numerous cited studies (Rowshandel, 2006; Baker, 2007; Tothong et al., 2007; Spudich and Chiou, 2008; Shahi and Baker, 2011) have been made possible thanks to the extensive NGA Project database, which

once again highlights the importance of the efforts on the accumulation and analysis of earthquake records.

The presented summary shows that quite much attention has been given to incorporating the directivity effects in the seismic hazard analysis. Various models have been created to estimate the impact of these effects on ground motion, and frameworks have been elaborated to incorporate them in the PSHA computations. It has been demonstrated that the increase in the estimates of seismic hazard in the near-fault zones due to the influence of directivity effects can be very significant.

Yet, there currently remain several debatable issues that do not find a consensus. Different researchers differently determine a magnitude threshold, above which directivity effects can be expected: the values vary $M > 6.0, 6.5, 7.0$. There is no consensus on the dimensions of spatial areas around faults, where directivity effects are expected. Furthermore, there is no consensus on whether it is broadband or narrowband models that describe more accurately the influence of directivity effects on ground motion. Evidently, with the acquisition of new data and after the models are updated, these issues will be resolved.

FUNDING

CONFLICT OF INTEREST

The authors declare that they have no conflicts of interest.

REFERENCES

Abdelmeguid, M., Zhao, C., Yalcinkaya, E., Gazetas, G., Elbanna, A., and Rosakis, A., Revealing the dynamics of the Feb 6th 2023 $M7.8$ Kahramanmaraş. Pazarcik earthquake: near-field records and dynamic rupture modeling, Preprint submitted to EarthArXiv, 2023. https://doi.org/10.31223/X5066R

Abrahamson, N.A., Seismological aspects of near-fault ground motions, *Proc. 5th Caltrans Seismic Research Workshop*, Sacramento: California Department of Transportation, 1998.

Abrahamson, N.A., Effects of rupture directivity on probabilistic seismic hazard analysis, *Proc. 6th Seismic Zonation Workshop*, Palm Springs, 2000, Oakland: Earthquake Engineering Research Inst., 2000.

Acarel, D., Cambaz, M.D., Turhan, F., Mutlu, A.K., and Polat, R., Seismotectonics of Malatya Fault, Eastern Turkey, *Open Geosci.*, 2019, vol. 11, no. 1, pp. 1098–1111.

Akkar, S., Yazgan, U., and Gülkan, P., Drift estimates in frame buildings subjected to near-fault ground motions, *J. Struct. Eng.*, 2005, vol. 131, no. 7, pp. 1014–1024.

Alavi, B. and Krawinkler, H., *Effects of Near-Fault Ground Motions on Frame Structures*, Tech. Rep. no. 138, the John A. Blume Earthquake Engineering Center, Stanford, 2001.

Anderson, J.C. and Bertero, V., Uncertainties in establishing design earthquakes, *J. Struct. Eng.*, 1987, vol. 113, no. 8, pp. 1709−1724.

Andrews, D.J., Rupture velocity of plane strain shear cracks, *J. Geophys. Res.*, 1976, vol. 81, no. 32, pp. 5679−5687.

Baez, J.I. and Miranda, E., Amplification factors to estimate inelastic displacement demands for the design of structures in the near field, *Proc. 12th World Conference on Earthquake Engineering,* 2000, Article ID 1561.

Baker, J.W., Quantitative classification of near-fault ground motions using wavelet analysis, *Bull. Seismol. Soc. Am.*, 2007, vol. 97, no. 5, pp. 1486−1501.
https://doi.org/10.1785/0120060255

Baltzopoulos, G., Luzi, L., and Iervolino, I., Analysis of near-source ground motion from the 2019 ridgecrest earthquake sequence, *Bull. Seismol. Soc. Am.,* 2020, vol. 110, no. 4, pp. 1495−1505.
https://doi.org/10.1785/0120200038

Baltzopoulos, G., Baraschino, R., Chioccarelli, E., Cito, P., and Iervolino, I., *Preliminary engineering report on ground motion data of the Feb. 2023 Turkey seismic sequence, V1.0, Earthquake Reports*, 2023.

Bertero, V., Mahin, S., and Herrera, R., Problems in prescribing reliable design earthquakes, *Proc. 6th World Conference on Earthquake Engineering*, New Delhi, 1977, vol. 2, pp. 1741−1746.

Bertero, V., Mahin, S., and Herrera, R., Aseismic design implications of near-fault San Fernando earthquake records, *Earthquake Eng. Struct. Dyn.*, 1978, vol. 6, no. 1, pp. 31−42.

Bhat, H.S., Dmowska, R., Rice, J.R., and Kame, N., Dynamic slip transfer from the Denali to Totschunda faults, Alaska: Testing theory for fault branching, *Bull. Seismol. Soc. Am.*, 2004, vol. 94, no. 6B, pp. S202−S213.
https://doi.org/10.1785/0120040601

Bommer, J., Akkar, S., and Drouet, S., Extending ground-motion prediction equations for spectral accelerations to higher response frequencies, *Bull. Earthquake Eng.,* 2012, vol. 10, no. 2, pp. 379−399

Bouchon, M., Bouin, M.-P., Karabulut, H., Toksöz, M.N., Dietrich, M., and Rosakis, A.J., How fast is rupture during an earthquake? New insights from the 1999 Turkey earthquakes, *Geophys. Res. Lett.,* 2001, vol. 28, no. 14, pp. 2723−2726.
https://doi.org/10.1029/2001GL013112

Dunham, E. and Archuleta, R., Evidence for a supershear transient during the 2002 Denali fault earthquake, *Bull. Seismol. Soc. Am.*, 2004, vol. 94, no. 6B, pp. S256−S268.

Dunham, E. and Bhat, H., Attenuation of radiated ground motion and stresses from three-dimensional supershear ruptures, *J. Geophys. Res.: Solid Earth,* 2008, vol. 113, no. B8, Article ID B08319.

NEHRP Guidelines for the Seismic Rehabilitation of Buildings, Reports FEMA 273 (Guidelines) and 274 (Commentary), Washington: Federal Emergency Management Agency, 1997.

Garini, E. and Gazetas, G., *Second Preliminary Report (8-2-23) Emergence of Fault Rupture, Accelerograms*, Greece: NTUA, 2023.

Giardini, D., Danciu, L., Erdik, M., Tümsa, M.B.D., Şeşetyan, K., Akkar, S., Gülen, L., and Zare, M., Seismic hazard map of the Middle East, *Bull. Earthquake Eng.,* 2018, vol. 16, no. 8, pp. 3567−3570.
https://doi.org/10.1007/s10518-018-0347-3

Gülerce, Z., Tanvir Shah, S., Menekşe, A., Arda Özacar, A., Kaymakci, N., and Önder Çetin, K., Probabilistic seismic-hazard assessment for East Anatolian fault zone using planar fault source models, *Bull. Seismol. Soc. Am.,* 2017, vol. 107, no. 5, pp. 2353−2366.
https://doi.org/10.1785/0120170009

Hall, J., Heaton, T., Halling, M., and Wald, D., Near-source ground motion and its effects on flexible buildings, *Earthquake Spectra,* 1995, vol. 11, no. 4, pp. 569−605.

Harris, R. and Day, S., Dynamics of fault interaction: Parallel strike-slip faults, *J. Geophys. Res.: Solid Earth*, 1993, vol. 98, no. B3, pp. 4461−4472

Iervolino, I., Chioccarelli, E., and Baltzopoulos, G., Inelastic displacement ratio of near-source pulse-like ground motions, *Earthquake Eng. Struct. Dyn.*, 2012, vol. 41, no. 15, pp. 2351−2357.
https://doi.org/10.1002/eqe.2167

Iervolino, I., Cito, P., Felicetta, C., Lanzano, G., and Vitale, A., Exceedance of design actions in epicentral areas: insights from the Shake Map envelopes for the 2016−2017 central Italy sequence, *Bull. Earthquake Eng.,* 2021, vol. 19, no. 13, pp. 5391−5414.
https://doi.org/10.1007/s10518-021-01192-z

International Federation of Digital Seismograph Networks, Turkish National Strong Motion Network, Department of Earthquake, Disaster and Emergency Management Authority. https://doi.org/. Cited February 13, 2023.
https://doi.org/10.7914/SN/TK

Iwan, W., Drift spectrum: Measure of demand for earthquake ground motions, *J. Struct. Eng.*, 1997, vol. 123, no. 4, pp. 397−404.

Kalkan, E. and Kunnath, S.K., Effects of fling-step and forward directivity on the seismic response of buildings, *Earthquake Spectra,* 2006, vol. 22, no. 2, pp. 367−390.

Kartal, R., Kadirioğlu, F., and Zünbül, S., Kinematic of east Anatolian fault and Dead Sea fault, *Proc. Aktif Tektonik Araştırma Grubu 17. Çalıştayı (ATAG 17)*, Antalya, 2013.

Luco, N. and Cornell, C., Structure-specific scalar intensity measures for near-source and ordinary earthquake ground motions, *Earthquake Spectra,* 2007, vol. 23, no. 2, pp. 357−392.

Mahin, S., Bertero, V., Chopra, A., and Collins, R., *Response of the Olive View Hospital Main Building During the San Fernando Earthquake*, Report No. UCB/EERC-76/22, Earthquake Engineering Research Center, University of California, Berkeley, 1976.

Makris, N. and Black, C., Dimensional analysis of bilinear oscillators under pulse-type excitations, *J. Eng. Mech.,* 2004, vol. 130, no. 9, pp. 1019−1031.

Malhotra, P., *M* 7.8 Turkey earthquake of February 6, 2023.
https://www.researchgate.net/publication/368306978_M_78_Turkey_Earthquake_of_February_6_2023

Mavroeidis, G.P. and Papageorgiou, A.S., A mathematical representation of near-fault ground motion, *Bull. Seismol. Soc. Am.,* 2003, vol. 93, no. 3, pp. 1099−1131.

Mavroeidis, G., Dong, G., and Papageorgiou, A., Near-fault ground motions, and the response of elastic and inelastic single degree- of-freedom (SDOF) systems, *Earth-*

quake Eng. Struct. Dyn., 2004, vol. 33, no. 9, pp. 1023–1049.

Mello, M., Bhat, H.S., Rosakis, A.J., and Kanamori, H., Reproducing the supershear portion of the 2002 Denali earthquake rupture in laboratory, *Earth Planet. Sci. Lett.*, 2014, vol. 387, pp. 89–96.

Mello, M., Bhat, H., and Rosakis, A., Spatiotemporal properties of Sub-Rayleigh and supershear rupture velocity fields: Theory and experiments, *J. Mech. Phys. Solids*, 2016, vol. 93, pp. 153–181.

Menun, C. and Fu, Q., An analytical model for near-fault ground motions and the response of SDOF systems, *Proc. 7th U.S. National Conf. on Earthquake Engineering*, Boston: Mira Digital Publ., 2002, Article ID 11.

Montaldo, V., Faccioli, E., Zonno, G., Akinci, A., and Malagnini, L., Treatment of ground-motion predictive relationships for the reference seismic hazard map of Italy, *J. Seismol.,* 2005, vol. 9, no. 3, pp. 295–316.
https://doi.org/10.1007/s10950-005-5966-x

Nutt, R.V., *Improved Seismic Design Criteria for California Bridges: Provisional Recommendations*, Report No. ATC-32, Applied Technology Council, Redwood City, California, 1996.

Rosakis, A., Samudrala, O., and Coker, D., Cracks faster than the shear wave speed, *Science,* 1999, vol. 284, no. 5418, pp. 1337–1340.

Rosakis, A., Abdelmeguid, M., and Elbanna, A., Evidence of early supershear transition in the Mw 7.8 Kahramanmaraş earthquake from near-field records, Preprint submitted to EarthArXiv, 2023.
https://doi.org/10.31223/X5W95G

Rousseau, C.-E. and Rosakis, A., Dynamic path selection along branched faults: Experiments involving sub-Rayleigh and supershear ruptures, *J. Geophys. Res.: Solid Earth*, 2009, vol. 114, no. B8, Article ID B08303.

Rowshandel, B., Incorporating source rupture characteristic into ground-motion hazard analysis models, *Seismol. Res. Lett.*, 2006, vol. 77, no. 6, pp. 708–722.

Shahi, Sh. and Baker, J., An empirically calibrated framework for including the effects of near-fault directivity in probabilistic seismic hazard analysis, *Bull. Seismol. Soc. Am.,* 2011, vol. 101, no. 2, pp. 742–755.
https://doi.org/10.1785/0120100090

Somerville, P., Magnitude scaling of the near fault rupture directivity pulse, *Phys. Earth Planet. Inter.*, 2003, vol. 137, nos. 1–4, pp. 201–212.

Somerville, P., Engineering characterization of near fault ground motion, *New Zealand Society for Earthquake Engineering Conference*, Wairakei, 2005.

Somerville, P., Smith, N., Graves, R., and Abrahamson, N., Representation of near-fault rupture directivity effects in design ground motions, and application to Caltrans bridges, *Proc. National Seismic Conf. on Bridges and Highways*, San Diego, 1995.

Somerville, P., Saikia, C., Wald, D., and Graves, R., Implications of the Northridge earthquake for strong ground motions from thrust faults, *Bull. Seismol. Soc. Am.*, 1996, vol. 86, no. 1B, pp. S115–S125.

Somerville, P., Smith, N., Graves, R., and Abrahamson, N., Modification of empirical strong ground motion attenuation relations to include the amplitude and duration effects of rupture directivity, *Seismol. Res. Lett.,* 1997, vol. 68, no. 1, pp. 199–222.
https://doi.org/10.1785/gssrl.68.1.199

Spagnuolo, E., Akinci, A., Herrero, A., and Pucci, S., Implementing the effect of the rupture directivity on PSHA for the city of Istanbul, Turkey, *Bull. Seismol. Soc. Am.,* 2016, vol. 106, no. 6, pp. 2599–2613.
https://doi.org/10.1785/0120160020

Spudich, P. and Chiou, B.S., Directivity in NGA earthquake ground motions: Analysis using isochrone theory, *Earthquake Spectra*, 2008, vol. 24, no. 1, pp. 279–298.

Taftsoglou, M., Valkaniotis, S., Karantanellis, E., Goula, E., and Papathanassiou, G., Preliminary mapping of liquefaction phenomena triggered by the February 6 2023 M7.7 earthquake, Türkiye/Syria, based on remote sensing data, *Zenodo*, uploaded February 23, 2023.
https://doi.org/10.5281/zenodo.7668401

Templeton, E., Baudet, A., Bhat, H.S., Dmowska, R., Rice, J.R., Rosakis, A.J., and Rousseau, C-E., Finite element simulations of dynamic shear rupture experiments and dynamic path selection along kinked and branched faults, *J. Geophys. Res.: Solid Earth,* 2009, vol. 114, no. B8, Article ID B08304.
https://doi.org/10.1029/2008JB006174

Tothong, P., Cornell, C.A., and Baker, J., Explicit directivity-pulse inclusion in probabilistic seismic hazard analysis, *Earthquake Spectra*, 2007, vol. 23, no. 4, pp. 867–891.
https://doi.org/10.1193/1.2790487

Uniform Building Code, Whittier: International Conference of Building Officials, 1997.

U.S. Geological Survey, M 7.8—Pazarcik Earthquake, Kahramanmaras Earthquake Sequence. https://earthquake.usgs.gov/earthquakes/eventpage/us6000jllz/ origin/detail. Cited February 13, 2023.

Zeng, H., Wei, S., and Rosakis, A., A travel-time path calibration strategy for back-projection of large earthquakes and its application and validation through the segmented super-shear rupture imaging of the 2002 Mw 7.9 Denali earthquake, *J. Geophys. Res.: Solid Earth*, 2022, vol. 127, no. 6, Article ID e2022JB024359.